X-ray and Cryo-electron Microscopy Structures of Monalysin Pore-forming Toxin Reveal Multimerization of the Pro-form

Philippe Leone, Cecilia Bebeacua, Onya Opota, Christine Kellenberger, Bruno Klaholz, Igor Orlov, Christian Cambillau, Bruno Lemaitre, Alain Roussel

THE JOURNAL OF BIOLOGICAL CHEMISTRY VOL. 290, NO. 21, pp. 13191–13201, May 22, 2015

X-ray and Cryo-electron Microscopy Structures of Monalysin Pore-forming Toxin Reveal Multimerization of the Pro-form*

Received for publication, February 19, 2015 and in revised form, April 3, 2015 Published, JBC Papers in Press, April 5, 2015, DOI 10.1074/jbc.M115.646109

Philippe Leone[‡§1], Cecilia Bebeacua[‡§1], Onya Opota[¶2], Christine Kellenberger[‡§], Bruno Klaholz[‖], Igor Orlov[‖], Christian Cambillau[‡§], Bruno Lemaitre[¶], and Alain Roussel[‡§3]

From the [‡]CNRS, Architecture et Fonction des Macromolécules Biologiques (AFMB), Unité Mixte de Recherche (UMR) 7257, 13288 Marseille, France, the [§]Aix-Marseille Université, Architecture et Fonction des Macromolécules Biologiques, UMR 7257, 13288 Marseille, France, the [¶]Global Health Institute, School of Life Sciences, École Polytechnique Fédérale Lausanne (EPFL), CH-1015 Lausanne, Switzerland, and the [‖]Centre for Integrative Biology (CBI), Department of Integrated Structural Biology, IGBMC (Institute of Genetics and of Molecular and Cellular Biology), CNRS, UMR 7104/INSERM U964/Université de Strasbourg, 1 rue Laurent Fries, 67404 Illkirch, France

Background: Monalysin is a β-barrel pore-forming toxin secreted by *Pseudomonas entomophila.*
Results: Monalysin structure belongs to the Aerolysin fold family but is devoid of receptor-binding domain; pro-Monalysin forms a stable 18-mer complex.
Conclusion: The delivery of 18 subunits may bypass the requirement of receptor-dependent concentration.
Significance: The functional mechanism of Monalysin differs from that of described Aerolysin family members.

β-Barrel pore-forming toxins (β-PFT), a large family of bacterial toxins, are generally secreted as water-soluble monomers and can form oligomeric pores in membranes following proteolytic cleavage and interaction with cell surface receptors. Monalysin has been recently identified as a β-PFT that contributes to the virulence of *Pseudomonas entomophila* against *Drosophila*. It is secreted as a pro-protein that becomes active upon cleavage. Here we report the crystal and cryo-electron microscopy structure of the pro-form of Monalysin as well as the crystal structures of the cleaved form and of an inactive mutant lacking the membrane-spanning region. The overall structure of Monalysin displays an elongated shape, which resembles those of β-pore-forming toxins, such as Aerolysin, but is devoid of a receptor-binding domain. X-ray crystallography, cryo-electron microscopy, and light-scattering studies show that pro-Monalysin forms a stable doughnut-like 18-mer complex composed of two disk-shaped nonamers held together by N-terminal swapping of the pro-peptides. This observation is in contrast with the monomeric pro-form of the other β-PFTs that are receptor-dependent for membrane interaction. The membrane-spanning region of pro-Monalysin is fully buried in the center of the doughnut, suggesting that upon cleavage of pro-peptides, the two disk-shaped nonamers can, and have to, dissociate to leave the transmembrane segments free to deploy and lead to pore formation. In contrast with other toxins, the delivery of 18 subunits at once, nearby the cell surface, may be used to bypass the requirement of receptor-dependent concentration to reach the threshold for oligomerization into the pore-forming complex.

Pore-forming toxins (PFTs)[4] are produced by a wide range of organisms, such as bacteria, insects, marine invertebrates, poisonous reptiles, and mammals, mostly for defense, attack, or signaling (1). PFTs are generally secreted as soluble monomers that diffuse toward the membrane of target cells. Recognition and binding to a specific receptor cause them to associate with the target membrane, form multimers, and undergo a conformational change, leading to the formation of an aqueous pore inserted in the membrane. PFTs are classified according to the type of secondary structure elements used to cross the lipid bilayer at the onset of pore formation (2). Hence, these toxins are usually divided into two categories: α-PFTs and β-PFTs.

The heptameric structure of the *Staphylococcus aureus* α-hemolysin pore was determined more than 15 years ago (3) and was until recently the only high resolution structure of a β-PFT in the membrane-inserted form. The ring-shaped complex resembles a mushroom, with the cap forming the extracellular domain and the stem forming the membrane-spanning region, in which each subunit contributes one β-hairpin. In the recent past, several structures of PFTs have been determined, but the structures of both the soluble and the pore forms are available for only a few: the α-PFT ClyA (4, 5) and the β-PFTs cytolysin (6, 7) and γ-hemolysin (8–10). Recently, the structures of Aerolysin mutants in their monomeric and heptameric forms have been determined by using a combination of x-ray crystallography, cryo-electron microscopy (cryo-EM), molecular dynamics, and computational modeling (11). It should be noted that contrary to the α-hemolysin pore, which displays a

* This work was supported by the French Infrastructure for Integrated Structural Biology (FRISBI) Grant ANR-10-INSB-05-01 and by Instruct as part of the European Strategy Forum on Research Infrastructures (ESFRI).
The atomic coordinates and structure factors (codes 4MKO and 4MKQ) have been deposited in the Protein Data Bank (http://wwpdb.org/).
The EM structure of Monalysin was deposited at the Electron Microscopy Data Bank (EMDB) with accession number EMD-2698.
[1] Both authors contributed equally to this work.
[2] Present address: Institute of Microbiology, University Hospital of Lausanne, 1011 Lausanne, Switzerland.
[3] To whom correspondence should be addressed. Tel.: 33-491-825-593; Fax: 33-491-266-720; E-mail: alain.roussel@afmb.univ-mrs.fr.

[4] The abbreviations used are: PFT, pore-forming toxin; cryo-EM, cryo-electron microscopy; SEC, size exclusion chromatography; MALS, multiangle laser light scattering; RI, refractive index; r.m.s.d., root mean square deviation; CPE, *Clostridium perfringens* enterotoxin.

mushroom shape, the Aerolysin pore looks like a rivet with a flat disk-shaped head.

In a previous study (12), we showed that Monalysin is a β-PFT from *Pseudomonas entomophila* secreted as a pro-protein that should be cleaved to become fully active. Indeed cleaved Monalysin was more active than pro-Monalysin. Nevertheless at high concentration (more than 10 nM), we were able to detect cytotoxic activity with the pro-Monalysin. The pro-Monalysin may be cleaved by proteases present at the surface of the cells. Many toxins are secreted by pathogenic organisms as inactive precursors, presumably to protect the producing cells from self-destruction or to increase the efficiency of delivery to the target cells. Activation of toxin precursors often involves proteolytic processing by enzymes produced either by the pathogen itself or by the host organism. Different effects resulting from proteolytic cleavage have been described for bacterial toxins. It is noteworthy that in the case of anthrax toxin, proteolysis at a furin-sensitive cleavage site removes a 20-kDa fragment from the N terminus (13), leaving a 63-kDa fragment bound to the receptor. In absence of the N terminus fragment, the bound fragment self-associates to form a ring-shaped heptameric prepore (14). Following this step, a large amphipathic loop from each monomer is believed to be inserted into the membrane, forming a β-hairpin, which generates a 14-stranded β-barrel pore (15) in a pH-dependent manner (16). Another example of proteolytic activation mechanism has been reported for Aerolysin. Pro-Aerolysin is released as a soluble dimeric precursor (17) that can bind to target cells through its specific receptor-binding domain (18). Pro-Aerolysin is activated by proteolytic cleavage, which releases a C-terminal peptide (19) and promotes the formation of the oligomeric pore structure (20). It has been shown recently that the Aerolysin C-terminal peptide also serves as a molecular chaperone because it promotes the folding of the protein soluble state (21).

Here, to explore the activation mechanism of Monalysin, we determined three crystal structures of Monalysin (pro and cleaved forms and an inactive mutant) as well as the cryo-EM reconstruction of the pro-Monalysin particle. Coupled with studies in solution using light scattering (SEC/MALS/UV/RI), our findings reveal that pro-Monalysin forms a stable 18-mer complex in solution composed of two disk-shaped nonamers held together by N-terminal swapping of the pro-peptides.

Experimental Procedures

Protein Expression, Purification, and Analysis—Expression and purification of recombinant pro-Monalysin were performed as described previously (22). Limited trypsinolysis (1:10 w/w) was performed for 15 min at room temperature, and the soluble and non-soluble fractions were separated by centrifugation at 15,000 × *g* for 5 min.

The sequence of the Monalysin mutant $M^{\Delta 102-170}$, in which the membrane-spanning domain was deleted and replaced with a Gly-Ser dipeptide linker, was cloned into the pETG-20A vector using the Mega-Primer technique. The production of $M^{\Delta 102-170}$ was performed with the same procedure as for pro-Monalysin. For crystallization trials, the purified $M^{\Delta 102-170}$ was concentrated to 8.6 mg ml^{-1}.

SEC/MALS/UV/RI Analysis—For the size exclusion chromatography (SEC) with on-line multiangle laser light scattering (MALS), absorbance (UV), and refractive index (RI) analysis, pure pro-Monalysin and $M^{\Delta 102-170}$ were concentrated to 2.0 and 2.3 mg ml^{-1}, respectively, and stored at 4 °C. Proteins were centrifuged (10,000 × *g* for 5 min) just before the experiment. Size exclusion chromatography was carried out on an Alliance 2695 HPLC system (Waters) using a Silica Gel KW804 column (Shodex) equilibrated in 10 mM Tris, pH 7.5, and 150 mM NaCl at a flow of 0.5 ml/min. Detection was performed using a triple-angle light scattering detector (Mini-DAWN TREOS, Wyatt Technology), a quasi-elastic light scattering instrument (DynaPro, Wyatt Technology), and a differential refractometer (Optilab rEX, Wyatt Technology).

Crystallization, Data Collection, and Processing—Crystallization and data collection of pro-Monalysin and tantalum derivative were performed as described previously (22). The cleaved Monalysin crystals were obtained at room temperature from drops in which pro-Monalysin was co-crystalized with 1.5 mM $HgCl_2$, and appeared after several months contrary to pro-Monalysin crystals that appeared within a few days (22). The crystals were flash-frozen with 15% glycerol in a nitrogen gas stream at 100 K. X-ray diffraction data were collected to 1.7 Å resolution on beamline ID14-4 at the European Synchrotron Research Facility (ESRF, Grenoble, France). The $M^{\Delta 102-170}$ crystals were obtained, using a Mosquito robot (TTP Labtech), from the Crystal Screens 1 condition number 20 (0.1 M sodium cacodylate, pH 6.5, 0.2 M calcium acetate, 18% PEG8000). They were flash-frozen with 10% glycerol in a nitrogen gas stream at 100 K. X-ray diffraction data were collected to 2.65 Å resolution on beamline ID29 at the ESRF. The data sets were integrated with XDS (23) and scaled with SCALA (24) from CCP4 Suite v6.3.0 (25). Data collection statistics are reported in Table 1.

Structure Solution and Refinement—The structure of pro-Monalysin was solved by the single-wavelength anomalous diffraction method using the tantalum derivative data set at 3.6 Å resolution. A nine-tantalum complex substructure was as described previously (22). The experimental phases were further improved by solvent flattening and histogram matching using SOLOMON (26) and DM (27) as implemented in SHARP (28). The partial model was then used for molecular replacement with the native pro-Monalysin data set at 2.85 Å resolution using MOLREP (29). The pro-Monalysin model was manually completed using Turbo-Frodo (30). The structures of cleaved Monalysin and $M^{\Delta 102-170}$ were solved by molecular replacement with MOLREP. Refinement was performed with autoBUSTER (31) using automated non-crystallographic symmetry restraints, and the structures were corrected with COOT (32). Model validations were done with Molprobity (33). Refinement statistics are reported in Table 1.

Cytolytic Assay—Cytolytic assay was performed according to previously published protocol (34). S2 cells (5.10^5) were washed twice and suspended in PBS and then mixed into 100 nM pro-Monalysin, 100 nM Monalysin mutant $M^{\Delta 102-170}$, or buffer (50 mM Tris, pH 8.0, 500 mM NaCl) in a 96-well plate. In a previous study (12), we showed that pro-Monalysin displayed lysis activity at concentrations higher than 10 nM. The pro-Monalysin may be cleaved by proteases present at the surface of the cell. To

assess cell lysis rate, cell density variation was monitored through measurement of $OD_{600\,nm}$ every 5 min, after a brief shaking, during 1 h at room temperature, using a Tecan microplate reader.

Electron Microscopy—3-μl samples were applied and incubated onto glow-discharged Quantifoil grids for 1 min and subsequently blotted for 3 s before plunging into liquid ethane for vitrification using a FEI Vitrobot. ~220 CCD images were collected under low dose conditions using a Tecnai F30 microscope with a field emission gun operated at 300 kV (IGBMC, Strasbourg, France) and a FEI Eagle 4Kx4K CCD camera at a magnification of 59,000× (1.92 Å/pixel at the specimen level), and over a range of nominal defocus values comprised between −2 and −3.5 μm. Defocus estimation and contrast transfer function (CTF) correction were carried out using FINDCTF2D (TIGRIS software from Timothy Grant, Imperial College London). 50,000 particles were automatically selected using the program Boxer from the EMAN2 package (35), extracted into boxes of 144,144, and combined into a dataset stack (Fig. 1*A*). The dataset was pretreated using the SPIDER package (36) and submitted to maximum likelihood classification and alignment (37) using the Xmipp package (38). The initial map was built from a visually selected class average representing a side-view imposing D9 symmetry (Fig. 1, *B* and *C*). The initial structure was then refined by three-dimensional maximum likelihood refinement and further refined by projection matching with an angular sampling of 5° using SPIDER. After refinement, a final structure was obtained at a resolution of approximately 17 Å as estimated by Fourier shell correlation and the half-bit threshold criterion (39) (Fig. 1*D*). The final reconstruction was built with ~12,000 particles after removal of most particles in a top-view orientation to compensate for their large over-representation and reduce preferential views effects and three-dimensional distortions. Molecular graphics and analyses were performed with the UCSF Chimera package (Resource for Biocomputing, Visualization, and Informatics at the University of California, San Francisco (supported by NIGMS P41-GM103311 through the National Institutes of Health)). The model/EM map or EM map/EM map fitting was performed by the option "fit in map" of the "volume" register. The difference map was calculated using Chimera. First, the x-ray structure was converted into a density map using the option "Fit into structure," with a target resolution and values comparable with that of the EM map. This command also fit the new map using the original EM volume. Then, maps were subtracted using the command: "vop subtract #1 #2 modelId #3" to produce the difference map presented here.

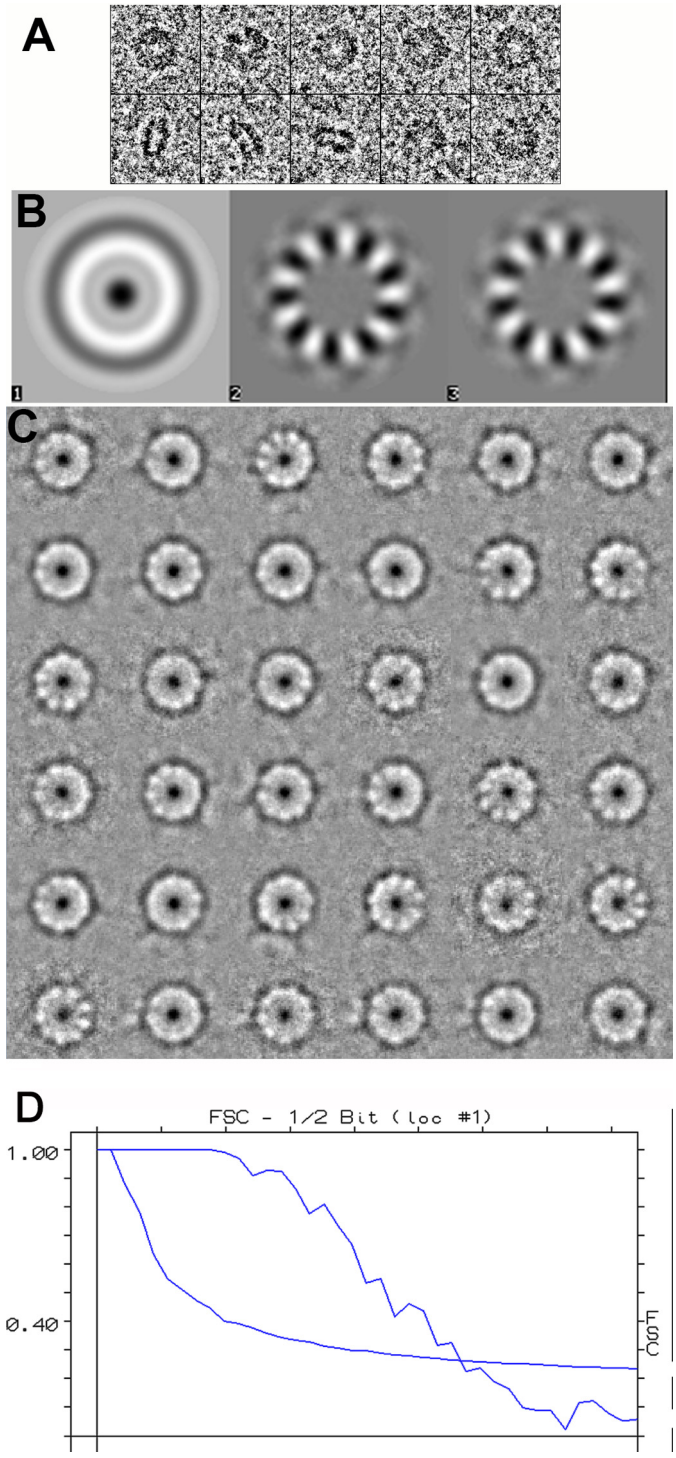

FIGURE 1. **Electron microscopy.** *A*, representative single particles of Monalysin 18-mer. *B*, eigenimages generated using multivariate statistical analysis (MSA) classification on the unaligned data set (48) with IMAGIC-5 software (49) exhibit a 9-fold symmetry present in the protein (images 2 and 3). *C*, some classes showing the 9-fold symmetry in top views. *D*, Fourier shell correlation (*FSC*) curves of the final three-dimensional reconstruction. These curves were obtained by correlation of two different three-dimensional images created by splitting the particles set into two subsets. The resolution was estimated by the half-bit cutoff threshold criterion as 17 Å.

Results

Crystal Structure of Inactive Full-length Pro-Monalysin—The pro-Monalysin protein crystallized in space group C2 with nine molecules in the asymmetric unit and an estimated solvent content of 53.5%. The structure was solved by the single-wavelength anomalous diffraction method using a tantalum derivative and was refined at 2.85 Å resolution (Table 1). Electron density was observed for residues 9–17 and 36–271 in all nine copies. The nine protomers are arranged as a disk-shaped complex resembling a conical washer. A symmetry-related disk stacks against the unique disk in the asymmetric unit, their two concave faces facing each other to form a doughnut-shaped 18-mer complex. This doughnut is 140 Å wide and ~80 Å thick, and its internal channel diameter is 30 Å (Fig. 2*A*). The pro-

TABLE 1
Data collection and refinement statistics

	pro-Monalysin	Tantalum derivative	Cleaved Monalysin	$M^{\Delta 102\text{-}170}$
Data collection				
Wavelength (Å)	0.87260	1.25452	0.93930	0.97887
Space group	C2	C2	$P2_12_12_1$	$P6_4$
a, *b*, *c* (Å)	162.4, 146.2, 144.4	160.7, 146.4, 147.0	64.9, 117.6, 150.6	129.5, 129.5, 78.9
β (°)	122.8	118.3		
Resolution (Å)[a]	30-2.85 (3.0-2.85)	30-3.6 (3.79-3.6)	30-1.7 (1.79-1.7)	30-2.65 (2.79-2.65)
Unique reflections[a]	65,957 (9,623)	34,322 (4,951)	126,982 (18,400)	21,936 (3,186)
Multiplicity[a]	3.4 (3.4)	6.2 (6.3)	6.7 (6.8)	3.4 (3.4)
Completeness (%)[a]	99.8 (99.9)	98.8 (98.6)	99.9 (100)	99.7 (99.6)
I/σ[a]	13.0 (2.1)	11.9 (2.2)	12.9 (3.9)	7.8 (2.0)
R_{merge} (%)[a,b]	9.5 (65.7)	12.8 (81.0)	9.3 (44.5)	13.2 (53.4)
Refinement and model quality				
Resolution (Å)	30–2.85		30–1.7	30–2.65
Reflections	65,948		126,896	21,920
R_{cryst}/R_{free} (%)[c]	18.2/21.6		17.9/20.4	18.7/21.6
Number of atoms				
Protein (number of copy in ASU)[d]	17,469 (9)		7,645 (4)	2,852 (2)
Water/ion/solvent	656/27/–[e]		1318/12/52	288/–/–[e]
Average B-factors (Å^2)				
Protein	71.8		14.9	50.6
Water/ion/solvent	49.4/82.7/–[e]		32.2/16.2/24.8	44.1/–/–[e]
r.m.s.d.[f]				
Bond (Å)	0.008		0.009	0.007
Angle (°)	0.99		0.93	0.93
Ramachandran plot (%)				
Most favored regions	97.3		98.2	95.7
Additionally allowed regions	2.7		1.8	4.3

[a] Values in parentheses are for the highest-resolution shell.
[b] $R_{merge} = \Sigma_{hkl}(\Sigma_i|I_{hkl} - \langle I_{hkl}\rangle|)/\Sigma_{hkl}|\langle I_{hkl}\rangle|$.
[c] $R_{cryst} = \Sigma_{hkl}||F_o| - |F_c||/\Sigma_{hkl}|F_o|$; R_{free} is calculated for 5% of randomly selected reflections excluded from refinement.
[d] ASU, asymmetric unit.
[e] Dashes indicate not applicable.
[f] Root mean square deviation from ideal values.

Monalysin monomer is an elongated molecule with overall dimensions of ~75 Å × 40 Å × 35 Å (Fig. 2*B*). Because an amino acid stretch was missing in the electron density map, we isolated protein samples from carefully washed crystals and analyzed them by SDS-PAGE to check the integrity of the crystallized material. A unique band corresponding to the full-length protein was observed, assessing the protein integrity (Fig. 3*A*, *lane 1*). We deduced thus that the N terminus segment (residues 9–17), visible in the electron density map (Fig. 2*C*), should be connected to the main protein domain through a polypeptide stretch not visible in the electron density map, probably due to disorder. However, it was not possible at this stage to determine the N terminus fragment connectivity as two residues at position 36, one from the same monomer and the other from a different monomer, are almost equidistant to residue 17 and are therefore equally good candidates for establishing connection (Fig. 2*D*). The N terminus segment (residues 9–17) contributes to about 40% of the buried surface area at the interface between the two nonamer disks as calculated by the Proteins, Interfaces, Structures and Assemblies (PISA) service at the European Bioinformatics Institute (40). The buried surface area between both nonamers is 14,444 Å^2 with the peptide as compared with 8,642 Å^2 when the peptide is omitted. The preferred dissociation pattern of the 18-mer given by PISA suggests separation of both nonamers as a first step. Accordingly, a band corresponding to the size of a nonamer is visible by SDS-PAGE analysis of recombinant pro-Monalysin (Fig. 3*B*, *lane 1*). A similar nonamer band is also found for the pro-Monalysin naturally secreted by *P. entomophila* (Fig. 3*B*, *lane 2*). This nonamer most probably results from the dissociation of an 18-mer entity, similar to that observed for the *Escherichia coli* recombinant protein.

Each protomer of full-length Monalysin possesses a central twisted β-sheet composed of three antiparallel β-strands (β3, β6, and β8/9) and flanked by the predicted pore-forming segment (12) and the C terminus region on either side (Fig. 2, *B* and *E*). The pore-forming domain (residues 102–170, *green* in Fig. 2, *B* and *E*), located between strands β3 and β6, forms two antiparallel β-strands connected by three α-helices, α3, α4, and α5. It is noteworthy that secondary structure prediction methods did not assign a helical secondary structure to the region encompassing α-helices α3, α4, and α5, suggesting that this region might have an equal propensity to form α or β secondary structures (Fig. 4). The C-terminal region forms a long α-helix followed by a small hairpin and a short α-helix. This latter helix, together with two hairpins located at one end of the central β sheet, forms the walls of a canyon that accommodates the N-terminal fragment (residues 9–17). This N terminus stretch buries 568 Å^2 of solvent-accessible surface on the protein core.

A structural similarity search within the Protein Data Bank using the pairwise structural comparison server DALI (41) of the Monalysin structure gave no statistically significant similarities, the highest Z-score being of 4.7 for an insecticidal crystal protein (Protein Data Bank (PDB) 4JP0) with a core r.m.s.d. of 4.6 Å. A protein sequence similarity retrieval using the BLAST program uncovered three genes with more than 30% of sequence identity with pro-Monalysin, from *Cystobacter fuscus* (48% sequence identity), *Pseudomonas putida* (35%), and *Pseudomonas* sp. (33%). They are annotated as hypothetical proteins

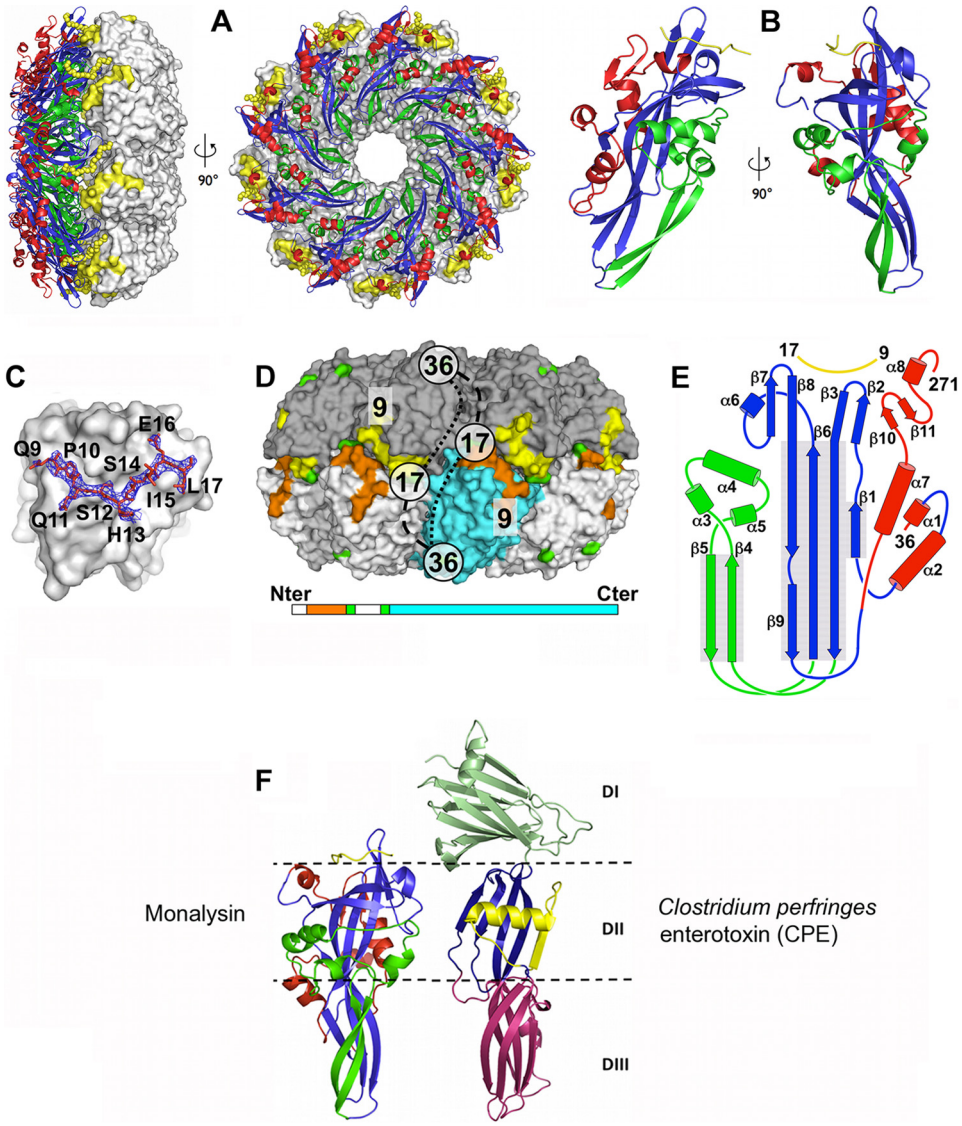

FIGURE 2. **X-ray structure of pro-Monalysin.** *A*, ribbon diagram and molecular surface of the pro-Monalysin 18-mer, viewed in two orientations rotated by 90° along the vertical axis. One disk of nine protomers is represented as a ribbon diagram (the central twisted β-sheet, the membrane-spanning region, the C terminus region, and the N terminus peptide are shown in *blue*, *green*, *red*, and *yellow*, respectively), and the other disk is represented as molecular surface colored in *gray* and *yellow* for the N terminus peptide. *B*, ribbon diagram of the pro-Monalysin monomer, viewed in two orientations rotated by 90° along the vertical axis. (same color code as in *A*). *C*, molecular surface of pro-Monalysin monomer with the peptide shown as *red sticks* and the electron density map shown in *dark blue*. The electron density map is contoured at 1σ. *D*, *upper panel*, the pro-Monalysin 18-mer is represented as a molecular surface. One disk of nine protomers is colored in *dark gray*, and the N terminus peptide (9–16) is in *yellow*. Residues 17 and 36 are colored in *green*. The other disk is shown in *gray*, except one protomer in *cyan*, with the N terminus peptide (9–16) and the residues 17 and 36 shown in *orange* and *green*, respectively. There are two possible ways to connect residue 17 to residue 36: inside the same protomer (*dots*) or between two facing protomers (*dashed lines*). *Lower panel*, a schematic representation of the sequence from the N terminus (*Nter*) to the C terminus (*Cter*) shows the relative location of the N terminus peptide (in *orange*), the residues 17 and 36 (in *green*), and the core of the protein (in *cyan*). *E*, schematic representation of the pro-Monalysin monomer using the same color code as in *B*. The β-strands and the α-helices are represented as *arrows* and *cylinders*, respectively. *F*, structural similarities between *C. perfringens* enterotoxin (CPE) and pro-Monalysin. Ribbon diagrams of CPE (in the same colors as in Kitadokoro *et al.* (46) and pro-Monalysin (in the same colors as in *A*) are shown. Domains I, II, and III of CPE (*DI*, *DII*, and *DIII*, respectively) are defined as in Kitadokoro *et al.* (46).

and hence remain with unknown function. The two last proteins are shorter because they lack the N terminus (Fig. 4).

Crystal Structure of the Cleaved, Active Form of Monalysin—Pro-Monalysin cleavage is required for the full activity of the toxin. In a previous study, we have shown that a shorter form of the protein could be obtained upon storage of samples at 4 °C for a long period of time (12). This processed form has a molecular mass of 26.5 kDa as determined by MALDI-TOF analysis, as opposed to 30.2 kDa for the full-length form. N-terminal Edman sequencing indicated that this processing occurred at the N terminus of Monalysin at residue 33 (12). The cleavage of the pro-Monalysin into its shorter form could also be induced by a limited trypsinolysis. It should be noted that for both methods, most of the protein precipitates and only less than 20% of the protein are found in the soluble fraction as estimated by concentration measurement using absorbance at 280 nm. Interestingly, SDS-PAGE analysis of the precipitated protein coming from both trypsin cleavage and long time storage showed the presence of high molecular mass multimeric forms resistant to SDS (Fig. 3*C*). Such high molecular mass bands have

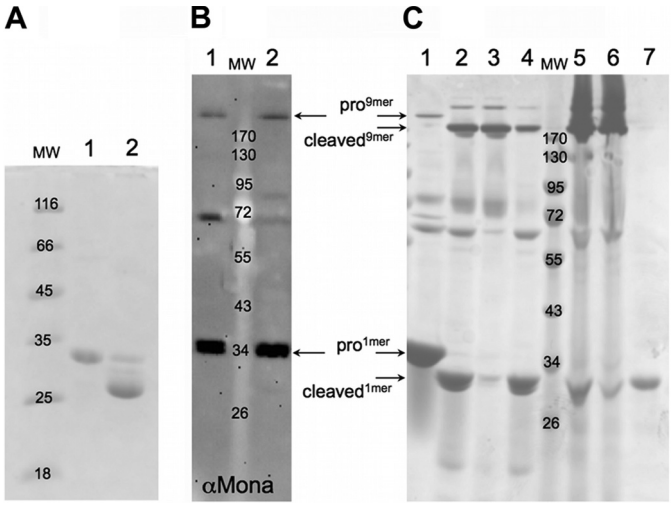

FIGURE 3. **Western blot and SDS-PAGE analysis of different Monalysin forms.** *A*, SDS page analysis of washed crystals of pro-Monalysin (*lane 1*) and washed crystals of cleaved Monalysin (*lane 2*). *MW*, molecular weight. *B*, Western blot analysis of pure recombinant pro-Monalysin (*lane 1*) and proteins from the filtrate supernatant of a *P. entomophila aprA* mutant overnight culture (*lane 2*) shows that Monalysin forms similar multimeric assemblies in both cases. The high molecular band above the 170-kDa marker may correspond to nonamers, the 18-mer being disrupted in the presence of SDS. The samples were not boiled to avoid complete multimer dissociation. Detection was done using guinea pig anti-pro-Monalysin antiserum (*αMona*). The *P. entomophila aprA* mutant was used to avoid cleavage of Monalysin by the metallo-protease AprA secreted by wild-type *P. entomophila*, as described previously (12). *C*, SDS page analysis of cleaved Monalysin shows the presence of high molecular bands corresponding to multimeric assemblies. *Lane 1*: pro-Monalysin; *lanes 2–4*: cleaved Monalysin obtained by trypsinolysis, total sample, pellet, and supernatant, respectively; *lanes 5–7*: cleaved Monalysin (sample stored for a long period of time), total sample, pellet, and supernatant, respectively. The samples were not boiled to avoid complete multimer dissociation.

been observed for Aerolysin after trypsin cleavage and were interpreted as evidence for pore formation (11). Interestingly, the high molecular mass band observed for the cleaved Monalysin is located just below the band corresponding to the pro-Monalysin nonamers (Fig. 3*C*), suggesting nonamer oligomerization for the pore. Crystals of the cleaved protein have been found incidentally in old crystallization drops of pro-Monalysin. Crystals appeared after more than 3 months and displayed a shape different from that of native crystals. SDS-PAGE analysis of these crystals showed a band corresponding to the cleaved form of Monalysin (Fig. 3*A*, *lane 2*). This new form crystallized in space group $P2_12_12_1$ with four molecules in the asymmetric unit. The structure was solved by molecular replacement with pro-Monalysin monomer and was refined at 1.70 Å resolution (Table 1). Electron density was observed for residues 36–271 in the four copies present in the asymmetric unit. The structure of the cleaved Monalysin fully superimposes to that of the pro-protein with an r.m.s.d. of 0.72 Å (Fig. 5*A*). As expected from the SDS-PAGE analysis, no density was observed in the N-terminal fragment-binding groove. The main difference between the pro-Monalysin and the cleaved protein arises from their oligomeric state. Although pro-Monalysin is an 18-mer complex both in solution and in the crystal, analysis of the soluble fraction of the cleaved protein by SEC/MALS/UV/RI revealed that it is monomeric in solution (Fig. 5*B*). The tetramer observed in the asymmetric unit is probably a crystallization artifact. However, as most (~80%) of the Monalysin precipitates upon cleavage, the physiological relevance of the monomeric soluble protein should be considered cautiously.

Crystal Structure of an Inactive Mutant of Monalysin Obtained by Deletion of the Membrane-spanning Region—An analysis of the pro-Monalysin structure, in combination with sequence alignment involving several β-PFTs of known structure, made it possible to define the membrane-spanning region of Monalysin as being located between residues 99 and 173 (12). In α toxin, a β-PFT from *Clostridium septicum*, deletion of the amphipathic loop disrupts the pore formation without affecting the fold of the toxin (42). To explore the role of the Monalysin pore-forming region, we generated four Monalysin mutants by deleting increasing lengths of the pore-forming region and accordingly named them $M^{\Delta 126-149}$, $M^{\Delta 124-151}$, $M^{\Delta 102-170}$, and $M^{\Delta 99-173}$. The largest deletion ($M^{\Delta 99-173}$) removed all the predicted membrane-spanning region, corresponding to more than a fourth of the protein. $M^{\Delta 102-170}$, the best expressed mutant, was produced and purified. SEC/MALS/UV/RI experiments indicate its tetrameric state in solution (Fig. 6*A*). As expected from our *in silico* analysis, $M^{\Delta 102-170}$ was found to lack any cytolytic activity on *Drosophila* S2 cells (Fig. 6*B*). Crystals of this inactive mutant $M^{\Delta 102-170}$ were obtained in space group $P6_4$ with two molecules in the asymmetric unit, and the structure was refined at 2.65 Å resolution (Table 1). Electron density was observed for residues 9–17, 36–101, and 171–271. The structure of the mutant was fully superimposable to that of the full-length protein with an r.m.s.d. of 0.86 Å (Fig. 6*C*). It is worth noticing that the N terminus fragment was found to bind to the rest of the molecule in a very similar way when compared with the pro-Monalysin structure. Furthermore, the excellent quality of the electron density map in this region for the $M^{\Delta 102-170}$ mutant made it possible to confirm the sequence assignment of the nine N-terminal residues. However, as for the pro-Monalysin structure, it was not possible to determine the connectivity of the N terminus fragment (Fig. 7).

Cryo-EM Structure of the Pro-Monalysin—We know that the 18–35 stretch is present in the crystals of pro-Monalysin but is not sufficiently ordered to give an interpretable electron density map. A careful analysis of the x-ray structure of the 18-mer shows that there are two possible paths for the polypeptidic chain to connect the residues 17 and 36. We thought that EM might reveal the presence of the slightly disordered 18–35 stretch. To this end, we performed cryo-EM-derived reconstruction of the wild-type toxin. The cryo-EM map exhibits a doughnut-like structure very close to that observed in the crystal structure (Fig. 8*A*). The 18-mer crystal structure of Monalysin fits extremely well within the EM density (cross-correlation coefficient = 0.67). Therefore, the results from three methods, analysis in solution by SEC/MALS/UV/RI, crystal structure, and single particle cryo-EM reconstruction, all point to pro-Monalysin as an 18-mer complex. The difference map calculated between the cryo-EM map and the molecular surface of the x-ray structure of the 18-mer revealed the location of the flexible polypeptide segment (residues 18–35) connecting the N terminus peptide to the rest of the molecule. A continuous density connects the N terminus fragment bound to a monomer coming from a first 9-mer half of the doughnut to a mono-

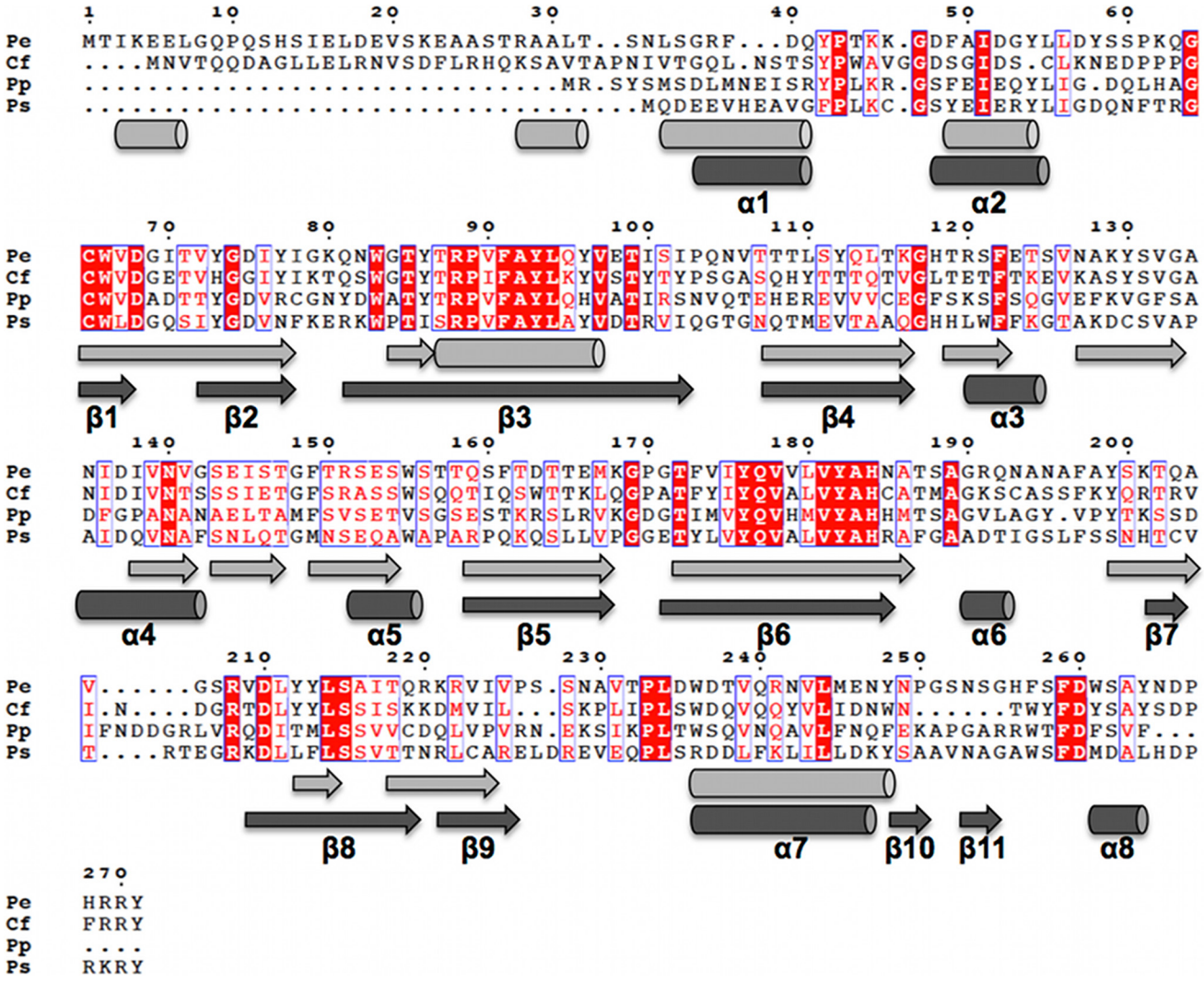

FIGURE 4. **Sequence of Monalysin and related proteins.** A multiple sequence alignment of Monalysin (*P. entomophila* (*Pe*)) and homologous proteins from *C. fuscus* (*Cf*), *P. putida* (*Pp*), and *Pseudomonas* sp (*Ps*) is shown. Monalysin numbering is displayed above. The secondary structure elements predicted by the JPRED server and observed in the crystal structure are represented below the alignment in *light gray* and *dark gray*, respectively.

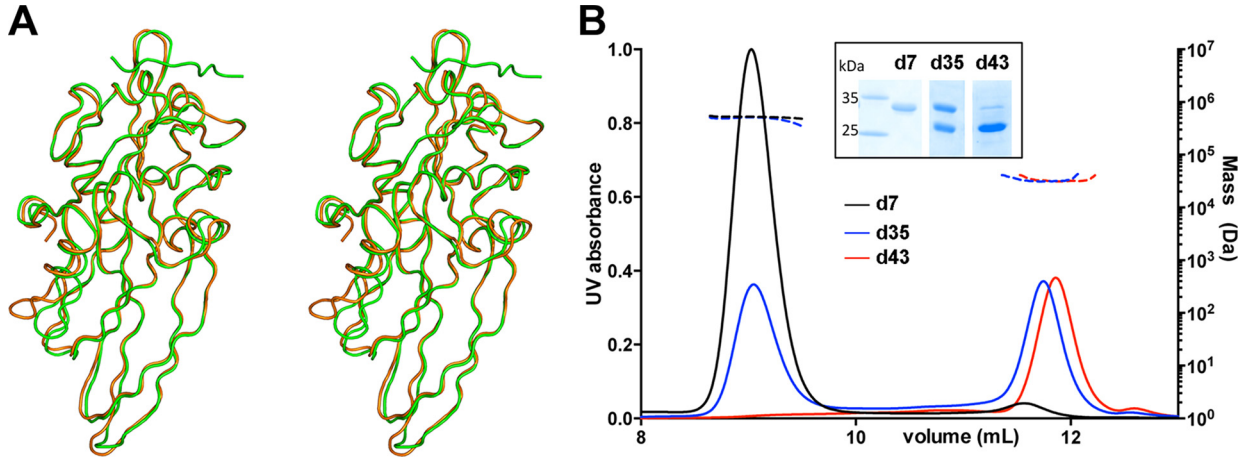

FIGURE 5. **Analysis of cleaved Monalysin.** *A*, the structure of pro-Monalysin (in *green*) is superposed to the structure of cleaved Monalysin (in *orange*). *B*, SEC/MALS/UV/RI analysis of pro-Monalysin over time, leading to cleaved Monalysin. Chromatograms of the soluble fraction of pro-Monalysin stored at 4 °C for 7 (*d7*), 35 (*d35*), and 43 (*d43*) days are shown in *black*, *blue*, and *red*, respectively. The molar mass (*right axis*) and the $UV_{280\ nm}$ absorbance (*left axis*) are plotted as a function of the column elution. The measured molar masses are ~500 and ~30 kDa for the first and second eluted peaks, respectively. *Inset*: SDS-PAGE of the samples used for SEC/MALS/UV/RI analysis (d7, d35, and d43).

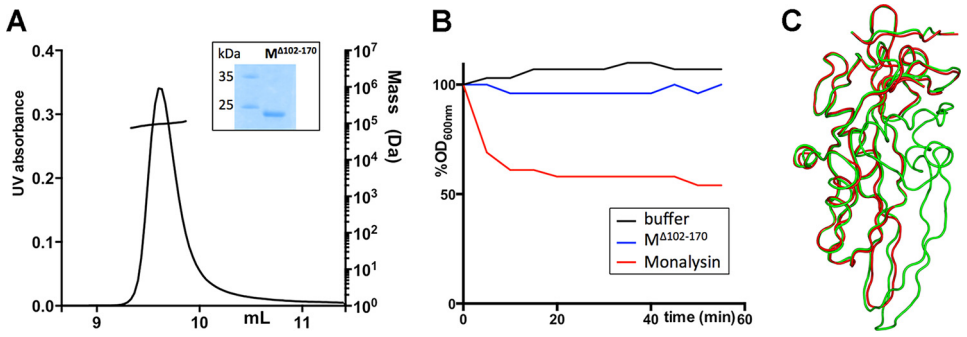

FIGURE 6. **Analysis of Monalysin mutant $M^{\Delta 102-170}$.** *A*, SEC/MALS/UV/RI analysis of Monalysin mutant $M^{\Delta 102-170}$. The molar mass (*right axis*) and the $UV_{280\ nm}$ absorbance (*left axis*) are plotted as a function of the column elution. The measured molar mass is ~93 kDa. *Inset*: SDS-PAGE of the sample used for SEC/MALS/UV/RI analysis. *B*, cytolytic activity of pro-Monalysin and Monalysin mutant $M^{\Delta 102-170}$ toward S2 cells. The $OD_{600\ nm}$ absorbance variation is plotted as a function of the time. The buffer used for protein purification served as a negative control. *C*, the structure of pro-Monalysin (in *green*) is superposed to the structure of the Monalysin mutant $M^{\Delta 102-170}$ (in *red*).

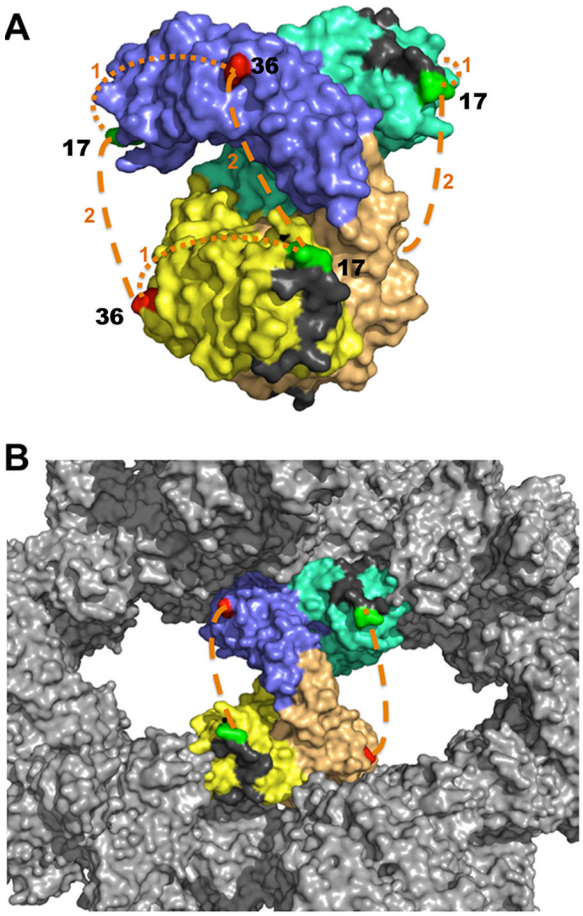

FIGURE 7. **Oligomeric structure of the Monalysin deletion mutant.** *A*, the tetrameric assembly of the Monalysin mutant. The Monalysin mutant $M^{\Delta 102-170}$ is tetrameric in solution as shown by SEC/MALS/UV/RI analysis but crystallizes with two molecules in the asymmetric unit. The tetrameric assembly was built using the PISA server (Krissinel and Henrick (40)). The molecular surfaces of the Monalysin mutants are colored in *blue* and *green* for the first asymmetric unit and in *yellow* and *light orange* for the second asymmetric unit. The residues 17 and 36 are colored in *green* and *red*, respectively. The N terminus peptides (residues 9–16) are colored in *dark gray*. As for the pro-Monalysin structure, it was not possible to determine the connectivity of the N terminus fragment. The two possible paths to link residue 17–36 are indicated by *orange square dots* (path number 1 within the same monomer) and *orange dashed line* (path number 2 between monomers belonging to two different asymmetric units). *B*, packing of the Monalysin mutant crystal. The tetrameric assembly of the Monalysin mutant (same colors as in *A*) is shown in the crystal packing (colored in *gray*). The path number 2 seems more favorable when considering the crystal packing.

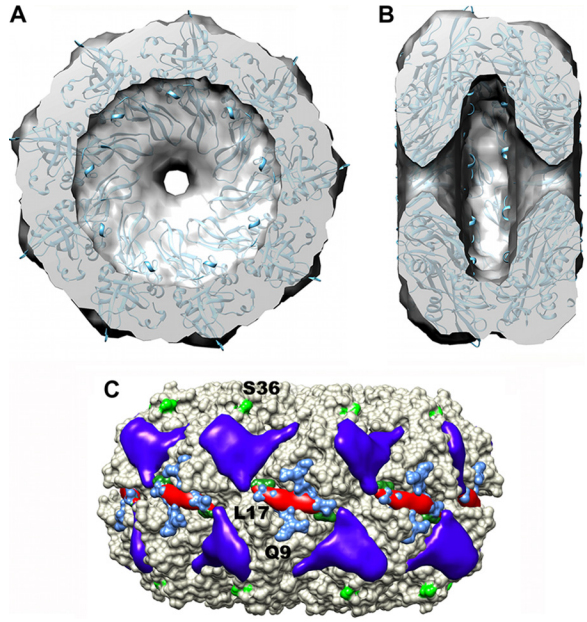

FIGURE 8. **The EM structure of Monalysin 18-mer.** *A*, fitting between the cryo-EM map (shown in *gray*) and the x-ray structure of pro-Monalysin 18-mer (shown as *blue colored ribbons*), viewed in two orientations rotated by 90° and slabbed at the nonamer junction level (on *left*) and at the center of the assembly (on *right*). *B*, the molecular surface of the pro-Monalysin 18-mer (crystal structure) is colored in *light gray* except for the residues 17 and 36, which are colored in *green*, and except for the N terminus peptides, which are colored in *light blue*. The difference map calculated between the cryo-EM map and the molecular surface of the x-ray structure of the pro-Monalysin 18-mer (without the N terminus peptide) is shown in *dark blue* (density corresponding to the missing linker region in the crystal structure, residues 18–35) and in *red* (density corresponding to the N terminus peptide).

mer coming from the other 9-mer (Fig. 8*B*). This domain swapping surely contributes to maintain the particle cohesion by establishing links between the two disk-shaped nonamers of the doughnut-like structure.

Discussion

Monalysin has been recently identified as a novel PFT that contributes to the virulence of *P. entomophila* against *Drosophila* (12). It has been shown that Monalysin requires N-terminal cleavage to become fully active, forms oligomers *in vitro*, and induces pore formation in artificial lipid membranes. The secondary structure prediction of the membrane-spanning

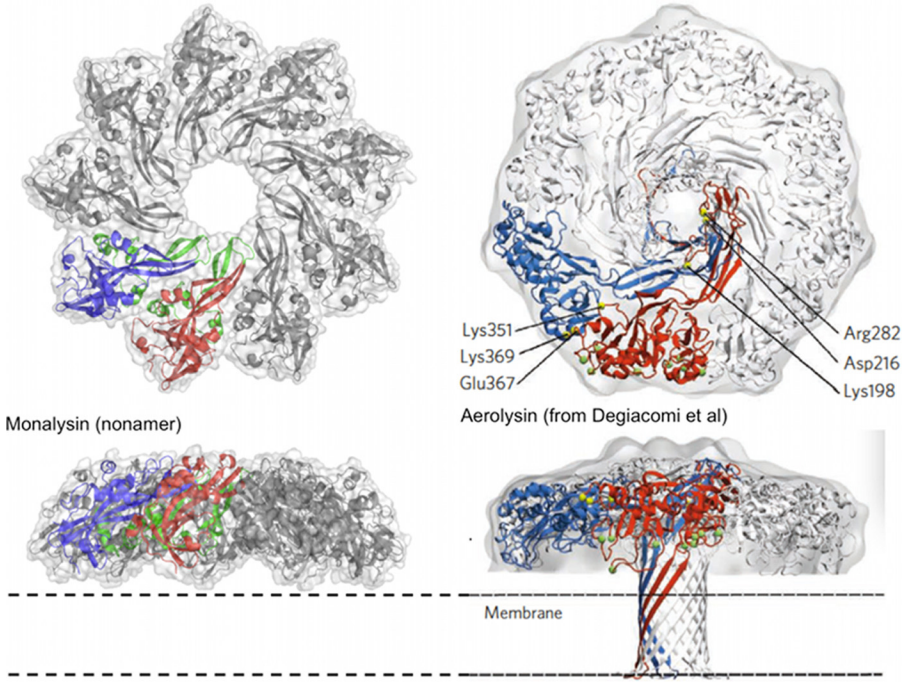

FIGURE 9. **Structural similarities between Monalysin nonamer and Aerolysin pore model (figure taken from Degiacomi *et al.* (11).**

domain indicated that Monalysin is a PFT of the β-type, and with the exception of this membrane-spanning domain, no sequence homology could be detected to any other described PFT. In the present study, we determined the structure of pro-Monalysin by x-ray crystallography and cryo-EM. We also determined the crystal structure of the cleaved form of Monalysin and of an inactive mutant lacking the membrane-spanning region. Finally, we analyzed the oligomerization state in solution using SEC/MALS/UV/RI.

The structure of Monalysin reveals similarity to the Aerolysin-like PFTs such as *Clostridium perfringens* ϵ-toxin (43), Aerolysin (44), LSL (lectin from *Laetiporus sulphureus*) (45), and *C. perfringens* enterotoxin (46), despite no detectable sequence homology. These toxins have an elongated shape, are formed of β-sheets, and gather three (or four) domains (Fig. 2*F*). Domain I (or domains I and II of Aerolysin) is responsible for binding to the respective toxin receptors. Domains II and III (or domains III and IV of Aerolysin) form the pore-forming domain itself, including a conserved core composed of four β-strands and the insertion β-hairpin (47). The structure of Monalysin displays this conserved core with two β-strands (β1/2 and β3 in Monalysin secondary structure numbering) followed by the putative membrane-spanning region (β4, α3, α4, α5, and β5) again followed by two additional β-strands (β6 and β8/9). Therefore, Monalysin structure belongs to the Aerolysin-like PFTs fold family but is devoid of obvious receptor-binding domain.

The structure of Monalysin is highly rigid, as shown by the three crystal structures solved in the present study, as they exhibit small r.m.s.d. values between each other. The structures of pro-Monalysin and cleaved Monalysin are highly similar, and strikingly, the deletion of more than a quarter of the residues of Monalysin (mutant $M^{\Delta 102-170}$) did not affect the fold of the core. This observation may suggest that the core structure of Monalysin does not change during pore formation and that conformational changes affect only the membrane-spanning region, as observed in α-hemolysin (3).

In the present study, x-ray crystallography and cryo-EM studies have shown that pro-Monalysin forms a stable 18-mer complex. A clear electron density was visible in the x-ray electron density map for the N-terminal fragment (residues 9–17). The location of the slightly flexible polypeptide segment (residues 18–35) connecting the N terminus peptide to the rest of the molecule was visible in the cryo-EM reconstruction and revealed the presence of a domain swapping that contributes to maintaining the particle cohesion and stability of the complex. Interestingly, the proteolytic cleavage necessary for the activation of the toxin occurs within this flexible segment.

An important difference between Monalysin and the other known members of the Aerolysin family is the absence of the domain responsible for cellular receptor binding (Fig. 2*F*). Although in other toxins receptors are used to concentrate the toxin to the cell surface, this mechanism may not apply to Monalysin. We suggest that, in contrast with other toxins, the delivery of 18 subunits at once, nearby the cell surface, may be used to bypass the requirement of receptor-dependent concentration to reach the threshold for oligomerization into the pore-forming complex. The structure of pro-Monalysin shows clearly that the membrane-spanning region is fully buried in the center of the doughnut (Fig. 2*A*) and therefore cannot enter in contact with the membrane of a target cell. Oligomerization may help to keep the toxin in a highly soluble form and would make it possible to convey a large amount of Monalysin from the production to the functional sites.

Very recently, Degiacomi *et al.* (11) obtained a near-atomistic model of the Aerolysin pore by using a combination of x-ray crystallography, cryo-EM, molecular dynamics, and computational modeling. Interestingly, the arrangement of the seven monomers of Aerolysin in the flat disk-shaped head of the pore

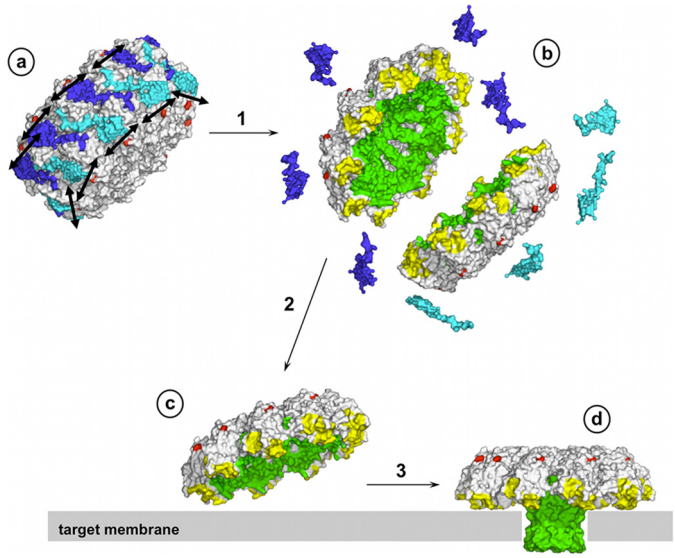

FIGURE 10. **Putative mechanism for the Monalysin activation and function.** Secreted pro-Monalysin oligomerizes in an inactive 18-mer (***a***). Upon proteolytic cleavage of the N terminus peptides (colored in *light* and *dark blue*) (**1**), the 18-mer structure dissociates into nonamers (***b***) that are recruited to the target membrane (**2**). Then, membrane-bound active nonamers (***c***) undergo oligomerization and conformational changes (**3**), leading to the formation of the pore (***d***).

structure resembles that of the nine monomers of Monalysin in the present structure (Fig. 9). To date, we have no data on the multimerization state of the Monalysin pore, but it is tempting to think that after cleavage, the 18-mer complex dissociates into two disk-shaped nonamers in which the transmembrane segments are unmasked and ready to engage the conformational change leading to the pore formation (Fig. 10). Further studies on the Monalysin are envisaged to answer questions concerning the pore formation, the recognition of the cell, and the prevention of self-attack.

Acknowledgments—We thank the European Synchrotron Research Facility (ESRF, Grenoble, France) and the Soleil synchrotron (Saint-Aubin, France), and in particular the staffs of beamlines ID23 and Proxima1, respectively, for their assistance.

Note Added in Proof—The legend for Fig. 1*B* was not correct in the version of this article that was published on April 5, 2015 as a Paper in Press. This error has been corrected. This correction does not change the interpretation of the results or the conclusions.

References

1. Parker, M. W., and Feil, S. C. (2005) Pore-forming protein toxins: from structure to function. *Prog. Biophys. Mol. Biol.* **88,** 91–142
2. Gouaux, E. (1997) Channel-forming toxins: tales of transformation. *Curr. Opin. Struct. Biol.* **7,** 566–573
3. Song, L., Hobaugh, M. R., Shustak, C., Cheley, S., Bayley, H., and Gouaux, J. E. (1996) Structure of staphylococcal α-hemolysin, a heptameric transmembrane pore. *Science* **274,** 1859–1866
4. Wallace, A. J., Stillman, T. J., Atkins, A., Jamieson, S. J., Bullough, P. A., Green, J., and Artymiuk, P. J. (2000) *E. coli* hemolysin E (HlyE, ClyA, SheA): x-ray crystal structure of the toxin and observation of membrane pores by electron microscopy. *Cell* **100,** 265–276
5. Mueller, M., Grauschopf, U., Maier, T., Glockshuber, R., and Ban, N. (2009) The structure of a cytolytic α-helical toxin pore reveals its assembly mechanism. *Nature* **459,** 726–730
6. De, S., and Olson, R. (2011) Crystal structure of the *Vibrio cholerae* cytolysin heptamer reveals common features among disparate pore-forming toxins. *Proc. Natl. Acad. Sci. U.S.A.* **108,** 7385–7390
7. Olson, R., and Gouaux, E. (2005) Crystal structure of the *Vibrio cholerae* cytolysin (VCC) pro-toxin and its assembly into a heptameric transmembrane pore. *J. Mol. Biol.* **350,** 997–1016
8. Olson, R., Nariya, H., Yokota, K., Kamio, Y., and Gouaux, E. (1999) Crystal structure of staphylococcal LukF delineates conformational changes accompanying formation of a transmembrane channel. *Nat. Struct. Biol.* **6,** 134–140
9. Roblin, P., Guillet, V., Joubert, O., Keller, D., Erard, M., Maveyraud, L., Prévost, G., and Mourey, L. (2008) A covalent S-F heterodimer of leucotoxin reveals molecular plasticity of β-barrel pore-forming toxins. *Proteins* **71,** 485–496
10. Yamashita, K., Kawai, Y., Tanaka, Y., Hirano, N., Kaneko, J., Tomita, N., Ohta, M., Kamio, Y., Yao, M., and Tanaka, I. (2011) Crystal structure of the octameric pore of staphylococcal γ-hemolysin reveals the β-barrel pore formation mechanism by two components. *Proc. Natl. Acad. Sci. U.S.A.* **108,** 17314–17319
11. Degiacomi, M. T., Iacovache, I., Pernot, L., Chami, M., Kudryashev, M., Stahlberg, H., van der Goot, F. G., and Dal Peraro, M. (2013) Molecular assembly of the aerolysin pore reveals a swirling membrane-insertion mechanism. *Nat. Chem. Biol.* **9,** 623–629
12. Opota, O., Vallet-Gély, I., Vincentelli, R., Kellenberger, C., Iacovache, I., Gonzalez, M. R., Roussel, A., van der Goot, F. G., and Lemaitre, B. (2011) Monalysin, a novel β-pore-forming toxin from the *Drosophila* pathogen *Pseudomonas entomophila*, contributes to host intestinal damage and lethality. *PLoS Pathog.* **7,** e1002259
13. Molloy, S. S., Bresnahan, P. A., Leppla, S. H., Klimpel, K. R., and Thomas, G. (1992) Human furin is a calcium-dependent serine endoprotease that recognizes the sequence Arg-*X*-*X*-Arg and efficiently cleaves anthrax toxin protective antigen. *J. Biol. Chem.* **267,** 16396–16402
14. Milne, J. C., Furlong, D., Hanna, P. C., Wall, J. S., and Collier, R. J. (1994) Anthrax protective antigen forms oligomers during intoxication of mammalian cells. *J. Biol. Chem.* **269,** 20607–20612
15. Benson, E. L., Huynh, P. D., Finkelstein, A., and Collier, R. J. (1998) Identification of residues lining the anthrax protective antigen channel. *Biochemistry* **37,** 3941–3948
16. Lacy, D. B., Wigelsworth, D. J., Melnyk, R. A., Harrison, S. C., and Collier, R. J. (2004) Structure of heptameric protective antigen bound to an anthrax toxin receptor: a role for receptor in pH-dependent pore formation. *Proc. Natl. Acad. Sci. U.S.A.* **101,** 13147–13151
17. van der Goot, F. G., Ausio, J., Wong, K. R., Pattus, F., and Buckley, J. T. (1993) Dimerization stabilizes the pore-forming toxin aerolysin in solution. *J. Biol. Chem.* **268,** 18272–18279
18. Gruber, H. J., Wilmsen, H. U., Cowell, S., Schindler, H., and Buckley, J. T. (1994) Partial purification of the rat erythrocyte receptor for the channel-forming toxin aerolysin and reconstitution into planar lipid bilayers. *Mol. Microbiol.* **14,** 1093–1101
19. van der Goot, F. G., Hardie, K. R., Parker, M. W., and Buckley, J. T. (1994) The C-terminal peptide produced upon proteolytic activation of the cytolytic toxin aerolysin is not involved in channel formation. *J. Biol. Chem.* **269,** 30496–30501
20. Cabiaux, V., Buckley, J. T., Wattiez, R., Ruysschaert, J. M., Parker, M. W., and van der Goot, F. G. (1997) Conformational changes in aerolysin during the transition from the water-soluble protoxin to the membrane channel. *Biochemistry* **36,** 15224–15232
21. Iacovache, I., Degiacomi, M. T., Pernot, L., Ho, S., Schiltz, M., Dal Peraro, M., and van der Goot, F. G. (2011) Dual chaperone role of the C-terminal propeptide in folding and oligomerization of the pore-forming toxin aerolysin. *PLoS Pathog.* **7,** e1002135
22. Blemont, M., Vincentelli, R., Kellenberger, C., Opota, O., Lemaitre, B., Roussel, A., and Leone, P. (2013) Crystallization and preliminary X-ray analysis of monalysin, a novel β-pore-forming toxin from the entomopathogen *Pseudomonas entomophila*. *Acta Crystallogr. Sect F Struct. Biol. Cryst. Commun.* **69,** 930–933
23. Kabsch, W. (2010) Integration, scaling, space-group assignment and post-refinement. *Acta Crystallogr. D Biol. Crystallogr.* **66,** 133–144

24. Evans, P. (2006) Scaling and assessment of data quality. *Acta Crystallogr. D Biol. Crystallogr.* **62,** 72–82
25. Winn, M. D., Ballard, C. C., Cowtan, K. D., Dodson, E. J., Emsley, P., Evans, P. R., Keegan, R. M., Krissinel, E. B., Leslie, A. G., McCoy, A., McNicholas, S. J., Murshudov, G. N., Pannu, N. S., Potterton, E. A., Powell, H. R., Read, R. J., Vagin, A., and Wilson, K. S. (2011) Overview of the CCP4 suite and current developments. *Acta Crystallogr. D Biol. Crystallogr.* **67,** 235–242
26. Abrahams, J. P., and Leslie, A. G. (1996) Methods used in the structure determination of bovine mitochondrial F1 ATPase. *Acta Crystallogr. D Biol. Crystallogr.* **52,** 30–42
27. Cowtan, K. D., and Zhang, K. Y. (1999) Density modification for macromolecular phase improvement. *Prog. Biophys. Mol. Biol.* **72,** 245–270
28. Bricogne, G., Vonrhein, C., Flensburg, C., Schiltz, M., and Paciorek, W. (2003) Generation, representation and flow of phase information in structure determination: recent developments in and around SHARP 2.0. *Acta Crystallogr. D Biol. Crystallogr.* **59,** 2023–2030
29. Vagin, A., and Teplyakov, A. (2010) Molecular replacement with MOLREP. *Acta Crystallogr. D Biol. Crystallogr.* **66,** 22–25
30. Roussel, A., and Cambillau, C. (1991) Turbo-Frodo, in *Silicon Graphics Geometry Partners Directory*, p. 86, Silicon Graphics, Mountain View, CA
31. Blanc, E., Roversi, P., Vonrhein, C., Flensburg, C., Lea, S. M., and Bricogne, G. (2004) Refinement of severely incomplete structures with maximum likelihood in BUSTER-TNT. *Acta Crystallogr. D Biol. Crystallogr.* **60,** 2210–2221
32. Emsley, P., Lohkamp, B., Scott, W. G., and Cowtan, K. (2010) Features and development of Coot. *Acta Crystallogr. D Biol. Crystallogr.* **66,** 486–501
33. Davis, I. W., Leaver-Fay, A., Chen, V. B., Block, J. N., Kapral, G. J., Wang, X., Murray, L. W., Arendall, W. B., 3rd, Snoeyink, J., Richardson, J. S., and Richardson, D. C. (2007) MolProbity: all-atom contacts and structure validation for proteins and nucleic acids. *Nucleic Acids Res.* **35,** W375–W383
34. Peterson, M. L., and Schlievert, P. M. (2006) Glycerol monolaurate inhibits the effects of Gram-positive select agents on eukaryotic cells. *Biochemistry* **45,** 2387–2397
35. Tang, G., Peng, L., Baldwin, P. R., Mann, D. S., Jiang, W., Rees, I., and Ludtke, S. J. (2007) EMAN2: an extensible image processing suite for electron microscopy. *J. Struct. Biol.* **157,** 38–46
36. Shaikh, T. R., Gao, H., Baxter, W. T., Asturias, F. J., Boisset, N., Leith, A., and Frank, J. (2008) SPIDER image processing for single-particle reconstruction of biological macromolecules from electron micrographs. *Nat. Protoc.* **3,** 1941–1974
37. Scheres, S. H. (2010) Classification of structural heterogeneity by maximum-likelihood methods. *Methods Enzymol.* **482,** 295–320
38. Scheres, S. H., Núñez-Ramírez, R., Sorzano, C. O., Carazo, J. M., and Marabini, R. (2008) Image processing for electron microscopy single-particle analysis using XMIPP. *Nat. Protoc.* **3,** 977–990
39. van Heel, M., and Schatz, M. (2005) Fourier shell correlation threshold criteria. *J. Struct. Biol.* **151,** 250–262
40. Krissinel, E., and Henrick, K. (2007) Inference of macromolecular assemblies from crystalline state. *J. Mol. Biol.* **372,** 774–797
41. Holm, L., and Rosenström, P. (2010) Dali server: conservation mapping in 3D. *Nucleic Acids Res.* **38,** W545–W549
42. Melton, J. A., Parker, M. W., Rossjohn, J., Buckley, J. T., and Tweten, R. K. (2004) The identification and structure of the membrane-spanning domain of the *Clostridium septicum* α toxin. *J. Biol. Chem.* **279,** 14315–14322
43. Cole, A. R., Gibert, M., Popoff, M., Moss, D. S., Titball, R. W., and Basak, A. K. (2004) *Clostridium perfringens* ϵ-toxin shows structural similarity to the pore-forming toxin aerolysin. *Nat. Struct. Mol. Biol.* **11,** 797–798
44. Parker, M. W., Buckley, J. T., Postma, J. P., Tucker, A. D., Leonard, K., Pattus, F., and Tsernoglou, D. (1994) Structure of the *Aeromonas* toxin proaerolysin in its water-soluble and membrane-channel states. *Nature* **367,** 292–295
45. Mancheño, J. M., Tateno, H., Goldstein, I. J., Martínez-Ripoll, M., and Hermoso, J. A. (2005) Structural analysis of the *Laetiporus sulphureus* hemolytic pore-forming lectin in complex with sugars. *J. Biol. Chem.* **280,** 17251–17259
46. Kitadokoro, K., Nishimura, K., Kamitani, S., Fukui-Miyazaki, A., Toshima, H., Abe, H., Kamata, Y., Sugita-Konishi, Y., Yamamoto, S., Karatani, H., and Horiguchi, Y. (2011) Crystal structure of *Clostridium perfringens* enterotoxin displays features of β-pore-forming toxins. *J. Biol. Chem.* **286,** 19549–19555
47. Szczesny, P., Iacovache, I., Muszewska, A., Ginalski, K., van der Goot, F. G., and Grynberg, M. (2011) Extending the aerolysin family: from bacteria to vertebrates. *PLoS One* **6,** e20349
48. van Heel, M. (1984) Multivariate statistical classification of noisy images (randomly oriented biological macromolecules). *Ultramicroscopy* **13,** 165–183
49. van Heel, M., Harauz, G., Orlova, E. V., Schmidt, R., and Schatz, M. (1996) A new generation of the IMAGIC image processing system. *J. Struct. Biol.* **116,** 17–24